

The nature of the Li enrichment in the most Li-rich giant star

Hong-Liang Yan^{1,2}, Jian-Rong Shi^{*1,2}, Yu-Tao Zhou^{1,2}, Yong-Shou Chen³, Er-Tao Li⁴, Suyalatu Zhang⁵, Shao-Lan Bi⁶, Ya-Qian Wu⁶, Zhi-Hong Li³, Bing Guo³, Wei-Ping Liu³, Qi Gao^{1,2}, Jun-Bo Zhang¹, Ze-Ming Zhou^{1,2}, Hai-Ning Li¹, and Gang Zhao^{†1,2}

¹Key Laboratory of Optical Astronomy, National Astronomical Observatories, Chinese Academy of Sciences, Beijing 100012, China

²School of Astronomy and Space Science, University of Chinese Academy of Sciences, Beijing 100049, China

³China Institute of Atomic Energy, Beijing 102413, China

⁴College of Physics and Energy, Shenzhen University, Shenzhen 518060, China

⁵College of Physics and Electronics Information, Inner Mongolia University for Nationalities 028000, China

⁶Department of Astronomy, Beijing Normal University, Beijing 100875, P. R. China

About 1% of giants^[1] have anomalously high Li abundances in their atmospheres, conflicting directly with the prediction of the standard stellar evolution models^[2]. This finding makes the production and evolution of Li in the Universe intriguing, not only in the sense of Big Bang nucleosynthesis^[3, 4] or the interstellar medium^[5], but also for the evolution of stars. Decades of efforts have been put into explaining why such extreme objects exist^[6, 7, 8], yet the origins of Li-rich giants are still being debated. Here we report the discovery of the most Li-rich giant known to date, with a very high Li abundance of 4.51. This rare phenomenon was observed coincidentally with another short-term event: the star is experiencing its luminosity bump on the red giant branch. Such a high Li abundance indicates that the star might be at the very beginning of its Li-rich phase, which provides a great opportunity to investigate the origin and evolution of Li in the Galaxy. A detailed nuclear simulation is presented with up-to-date reaction rates to recreate the Li enrichment process in this star. Our results provide tight constraints on both observational and theoretical points of view, suggesting that low-mass giants can internally produce Li to a very high level through ⁷Be transportation during the red giant phase.

Lithium is too fragile to survive in deeper layers of a stellar atmosphere due to the high temperature. Thus the first dredge up (FDU) process can sharply dilute the surface Li abundance in red giants. This explains why the first discovery^[9] of a Li-rich giant evoked great interests on exploring and understanding the Li-rich objects. However, only about 150 Li-rich giants have been found^[1, 10, 11, 12, 13, 14] in the past three decades, and ~ 20 of them were found to be super Li-rich with Li abundances higher than 3.3. Considering the NLTE correc-

tions, three^[12, 15, 16] stars were found to be at a level of $A(\text{Li}) > 4.0$. Such rare objects could provide a great opportunity to reveal the nature of the phenomenon of Li-richness because high Li abundance cannot be maintained for a long time due to frequent convection activity. Taking advantage of the powerful ability for spectral collection with the Large Sky Area Multi-Object Fiber Spectroscopy Telescope (LAMOST), we have obtained a large sample of Li-rich candidates by measuring the equivalent width of the Li I line at $\lambda = 6707.8 \text{ \AA}$. One of our candidates, TYC 429-2097-1, has a super strong Li absorption line (see Fig. 1, panel a). We then made a follow-up high-resolution observation with the 2.4-m Automated Planet Finder Telescope (APF) located at Lick Observatory on June 23, 2015. The spectrum covers a wavelength range of 374 nm – 970 nm with a resolution of $\sim 80,000$. The total integration time was 1.5 hours and was divided into three single exposures (30 minutes each) for a better subtraction of cosmic-rays. The spectrum of TYC 429-2097-1 obtained from APF is presented in Fig. 1, panels (b) and (e), where the spectrum of HD 48381 is also plotted with a vertical shift of +0.3 as a comparison. HD 48381 is a star selected from the Gaia-ESO survey DR2, which has very similar stellar parameters to TYC 429-2097-1.

We used the spectroscopic method to derive the stellar parameters (see the ‘methods’ section for details). We presented the final derived parameters of TYC 429-2097-1 and the estimated errors in Table 1. The NLTE Li abundances for 6707.8 Å, 6103.6 Å, and 8126.3 Å are 4.42 ± 0.09 , 4.51 ± 0.09 , and 4.60 ± 0.08 , respectively. The averaged Li abundance is $A(\text{Li})_{\text{NLTE}} = 4.51 \pm 0.09$. Compared to previous studies, TYC 429-2097-1 has the highest Li abundance among all Li-rich giants ever discovered (see Fig. 2). The Li abundance in TYC 429-2097-1 is about 1,000 times as high as the widely-used Li-rich ‘standard’ of $A(\text{Li})=1.5$ (the lower purple dashed line in Fig. 2), despite this ‘standard’ being suggested to be luminosity-dependent^[24]. It is also about 15 times as high as me-

*sjr@nao.cas.cn

†gzhao@nao.cas.cn

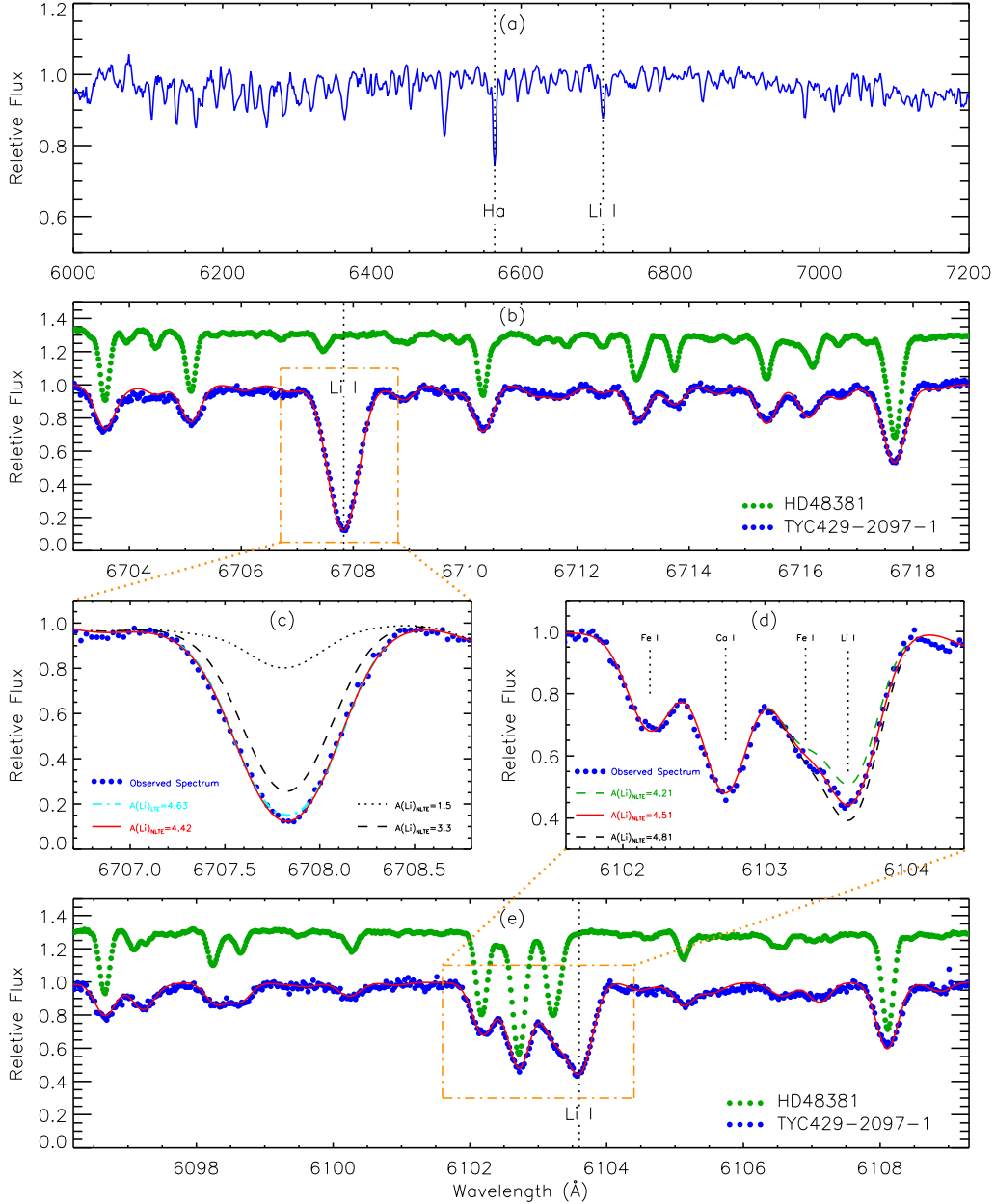


Figure 1: The observed spectra and line profile fittings for TYC 429-2097-1. The low-resolution spectrum from LAMOST is shown in panel (a), where H α line and Li I resonance line are indicated. Panels (b) and (e) display the high-resolution spectrum (blue dot) observed by APF near 6708 Å and 6103 Å, respectively. The spectrum of HD 48381 is also plotted (green dots) for comparison in both panel. The best profile fittings for these two lines are indicated with the red solid line in panels (c) and (d), respectively, where several profiles computed with different Li abundances are also presented. The profile from LTE calculation reaches saturation (cyan curve) in panel (c), and increasing Li abundance will barely affect the computed profile, therefore the LTE abundance shown in panel (c) is estimated from the equivalent width of this line.

teoritic Li abundance (the upper purple dashed line in Fig. 2), which is thought to be the initial Li abundance for newly-formed young stars.

Although Li-rich giants were reported at various stages, such as RGB and core He-burning phases^[25], the Li-rich phase is likely to be a short-term event. An extremely Li-rich giant (possibly newly enriched) with rigorous investigation on its evolutionary stage would be definitely important. The location of the star was derived by the maximum likelihood method using the observed parameters (in this case, T_{eff} , $\log g$, and $[\text{Fe}/\text{H}]$ derived from the spectroscopic method) and a grid of evolutionary mod-

els computed with the MESA code (see the ‘method’ section for details). The derived luminosity and mass are $\log(L/L_{\odot})=1.95$ and $M=1.43 M_{\odot}$, respectively. We used the parallax of Gaia DR1^[26] to test the reliability of the information derived from the maximum likelihood method independently. The luminosity obtained from Gaia data leads to a very similar result of $\log(L_{\text{Gaia}}/L_{\odot})=2.00$. The mass was tested in the sense that if the mass is well determined, the surface gravity from Gaia parallax will show good consistency with the spectroscopic $\log g$ of 2.25. As expected, the final result is $\log g_{\text{Gaia}}=2.23$. Thus, we consider that the results derived from the maximum like-

Table 1: The key information of TYC 429-2097-1

Property		Value
Name		TYC 429-2097-1
T_{eff}	(K)	4696 ± 80
$\log g$		2.25 ± 0.10
$[\text{Fe}/\text{H}]$		-0.36 ± 0.06
ξ_t	(km s^{-1})	2.30 ± 0.10
$A(\text{Li})_{\text{NLTE}}$		4.51 ± 0.09
Gaia parallax π	(milli-arcsec)	0.73 ± 0.24
Mass	(M_{\odot})	$1.43^{+0.55}_{-0.54}$
$\log(L/L_{\odot})$		$1.95^{+0.25}_{-0.19}$
$\log(L_{\text{Gaia}}/L_{\odot})$		2.00 ± 0.06
$\log g_{\text{Gaia}}$		2.23 ± 0.16
$^{12}\text{C}/^{13}\text{C}$		12.0 ± 3.0
$v \sin i$	(km s^{-1})	11.3 ± 1.5
$[\alpha/\text{Fe}]$		0.19 ± 0.04

likelihood method are reliable, allowing us to robustly locate this star on the Hertzsprung-Russell diagram (H-R diagram) along with the corresponding MESA tracks (see Supplementary Figure 1). The star is likely occupying the region of the RGB-bump, a stage in which the μ -barrier is destroyed and the enhanced ‘extra-mixing’ might be ongoing inside the star. In addition, we also estimated the $^{12}\text{C}/^{13}\text{C}$ ratio as it has been suggested that the extra mixing will cause a decrease of $^{12}\text{C}/^{13}\text{C}$ to the range of 10 – 20. We found that the $^{12}\text{C}/^{13}\text{C}$ ratio in this star is 12.0 ± 3.0 , which is well within the predicted range. All the results obtained above are shown in Table 1.

It has long been suggested that the Li enrichment could be due to contaminations by external sources in the environment, such as the engulfment of a substellar component^[27] (e.g. giant planets or brown dwarfs) and the accretion from a Li-rich companion or diffuse medium. Yet the contribution from external sources is not infinite, since the contributor itself has a limited amount of Li, typically not higher than 3.3. A simulation on engulfment of a Jovian planet suggested that a typical upper limit for enrichment by such way is ~ 2.2 ^[23]. Our star has a much higher Li abundance than any of those values, thus it is very unlikely that the overabundant Li comes from the direct contribution of external sources.

The internal production of Li, on the other hand, is based on the Cameron–Fowler mechanism^[28] (CF mechanism). The production of ^7Be takes place where the temperature is too high to preserve the newly synthesized ^7Li , hence ^7Be must be transported quickly to the cooler region to form Li. This scenario would potentially require the low-mass giants to evolve to the RGB-bump, where the mean molecular weight discontinuity (or μ -barrier, a mass gradient caused by FDU) is erased. Meanwhile, it would need the presence of deep, enhanced ‘extra mixing’ (EM) to increase the depth and efficiency of the convective circulation, which in-turn alters the $^{12}\text{C}/^{13}\text{C}$ into

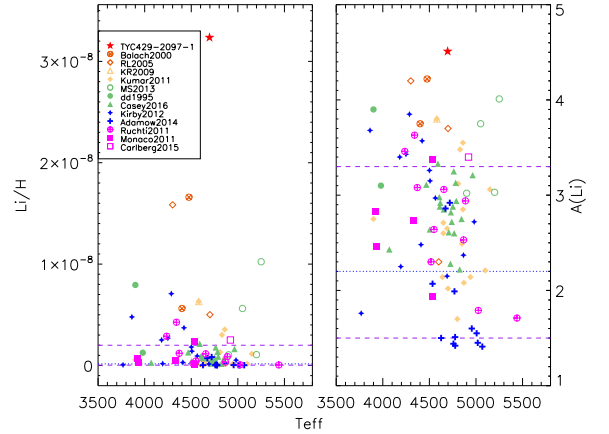


Figure 2: The distribution of Li-rich giants in T_{eff} - Li/H plane (left panel) and T_{eff} - $A(\text{Li})$ plane (right panel). TYC 429-2097-1 is indicated with a red star. The cited data are from different literatures as illustrated in the left panel, namely: Monaco2011^[10], Kirby2012^[11], MS2013^[12], Adamow2014^[13], Casey2016^[14], Balach2000^[15], RL2005^[16], Kumar2011^[17], dd1995^[18], KR2009^[19], Ruchti2011^[20], and Carlberg2015^[21]. All the Li abundances adopted here are based on NLTE calculations. If the original work did not perform the NLTE abundance analysis, we applied the NLTE corrections interpolated from Lind’s grid^[22] to the original LTE abundances. The horizontal dashed lines in purple indicate $A(\text{Li})=1.5$ and $A(\text{Li})=3.3$, respectively. The dotted blue line shows the upper limit of Li enriched by engulfment of a giant planet^[23].

a lower level than that after FDU. The observational features on both the evolutionary stage and $^{12}\text{C}/^{13}\text{C}$ ratio of our star coincide with these predictions remarkably well, but the limitation of self-production still remains unknown in the sense that none of the quantitative calculations with a nuclear reaction network has been presented to obtain such high amount of Li before. To test this speculation, we have made such simulation with a series of parameters. By using the RGB stellar structure as the input for the EM calculation, with the updated nuclear reaction rates and the asymmetric parameters of the EM model, we found that $A(\text{Li})$ in the envelope can exceed 4.0 for the processed material when the mass circulation finished. Our EM calculation with parameters of $\dot{M} = 52$, $\Delta=0.15$, $f_d=0.9$ and $f_u=0.1$ (see the ‘methods’ section for the details) yields $A(\text{Li})= 4.506$, where \dot{M} is the rate of mass transport in units of $10^{-6} M_{\odot} \text{ yr}^{-1}$, Δ is $\log T_H - \log T_p$, where T_H is the temperature at which the energy released from the H-burning shell reaches maximum and T_p is the maximum temperature sampled by the circulating material, and f_d and f_u are the fractional areas of the ‘pipes’ occupied by the mass flows moving downward and upward, respectively, and their values satisfy $f_d + f_u = 1$. This reproduces the observed Li abundance for TYC 429-2097-1 well. Repeating the same calculation with the alternative set of nuclear reaction rates from the JINA database^[29] yields a similar abundance of $A(\text{Li})= 4.515$. As a con-

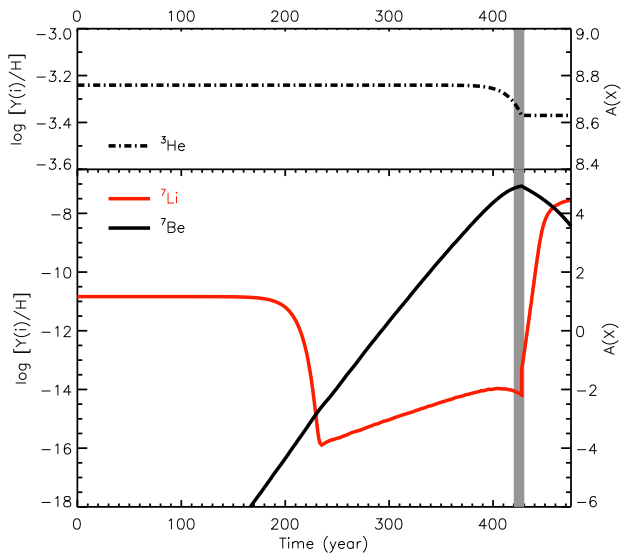


Figure 3: The calculated surface abundances and mass fraction of ^3He , ^7Be and ^7Li as functions of the processing time for the mass circulation. The left-hand y-axis indicates the mass fractions in logarithmic scale and the right-hand y-axis indicates the logarithmic abundances. The initial time is set to be zero when the sample material at the base of the envelope starts the mass circulation. The vertical solid line indicates the boundary between the downward and upward motion of the processed material. The yield of ^7Be reaches maximum by the end of the downward motion at $t=423$ yrs, and then ^7Li begins to dominate during the upward motion of the sample material for 47 yrs.

trast, assuming this star had never experienced any EM, the Li abundance would be constant at the initial value of $A(\text{Li})=1.16$, because the temperature in the envelope is too low to ignite both the production and destruction reactions of ^7Li . The abundances of ^3He , ^7Li and ^7Be as functions of the processing time for the mass circulation are shown in Fig. 3.

During the EM process, ^3He is converted to ^7Be via the reaction of $^3\text{He}(^4\text{He}, \gamma)^7\text{Be}$, and then ^7Be is quickly converted to ^7Li via the reaction of $^7\text{Be}(e^-, \nu)^7\text{Li}$. To achieve such high level of Li abundance, abundant ^3He is required. The initial surface ^3He is computed from the MESA model, which is $Y(^3\text{He}) = 4.038 \times 10^{-4}$. Fig. 3 shows the decrease of ^3He as a function of the time for EM processing. A total amount of $Y(^3\text{He})/\text{H} \sim 1.477 \times 10^{-4}$ is burned-off during this circulation, and the produced $Y(^7\text{Li})/\text{H}$ is 3.206×10^{-8} . This is because another reaction, $^3\text{He}(^3\text{He}, 2p)^4\text{He}$, dominates over the reaction $^3\text{He}(^4\text{He}, \gamma)^7\text{Be}$, thus consuming the majority of ^3He . The strong competition from $^3\text{He}(^3\text{He}, 2p)^4\text{He}$ reaction prevents more ^3He from converting to ^7Li . Testing with different sets of EM parameters shows that the maximum of Li abundance from our network calculation is 5.07. The ^3He supply may eventually run out and cannot be renewed by the giant, then the surface Li abundance is likely to decrease, even if the internal conditions remain the same. On the other hand, if the internal conditions do change, the surface Li abundance may also decline due to the destruction by convective activities in stars. Either way, the super Li-rich phase may disappear after a

short period of time. In our calculation, the *asymmetric* mass circulation described by a large ratio of f_d/f_u is a key factor for achieving super high Li-enrichment. This large f_d/f_u ratio indicates that the upward flow is moving much faster (since its ‘pipe’ is thinner) than the downward flow, while the mass is conservative in the EM process.

The cause of the EM has not been well understood, and rotationally induced mixing is often attempted. Indeed, TYC 429-2097-1 is a slightly rapid rotator with a projective velocity of 11.3 km s^{-1} , which is about ten times faster than that for normal giants. The spinning up of an RGB star is either caused by the tidal synchronization effects in a close binary system or the engulfment of a massive planet^[7, 27]. We calculated the radial velocities based on the two independent observations through LAMOST and APF (with an interval of 10 months), and found no significant radial velocity change at a level of a few kilometers per second, which is the typical uncertainty for the RV derived from LAMOST spectra. Thus it is very unlikely that a star has a stellar companion which is massive and close enough to spin up via tidal synchronization. On the other hand, one would expect some associated features that are detectable if a massive planet was engulfed and digested. For example, it was found that there might be a large probability for Li-rich giants exhibiting excess in the infrared (IR) flux, yet we found no sign of IR excess (see Supplementary Figure 2). In addition, if the matter exchange did happen at a certain time, there should be some fluctuations in the abundance pattern. However, TYC 429-2097-1’s $^{12}\text{C}/^{13}\text{C}$ is at a typical level for its stage^[7], and its α -abundance is also quite normal among the giants with similar $[\text{Fe}/\text{H}]$. Given all these facts, we speculate that in our case, the enhanced extra mixing might neither be caused by the presence of a massive planet (if there were any) nor a close stellar companion. There are other assumptions often approximated as the *internal* cause of enhanced extra mixing, i.e., thermohaline instabilities and magnetic buoyancy. The thermohaline convection driven by the $^3\text{He}(^3\text{He}, 2p)^4\text{He}$ reaction which produces a local depression in the mean molecular weight^[8] can cause enhanced extra mixing inside the star. The magnetic buoyancy mechanism in the presence of a magnetic dynamo would permit the buoyancy of magnetized material near the H-burning shell, thus inducing the form of matter circulation in RGB stars^[30]. We speculate that the magnetic buoyancy and thermohaline instabilities might play roles together during the mass circulation, in which the former may lead to very fast upward circulation and the latter drive downward circulation at a much slower speed.

Although the Li abundance measured in this star is super high, it is still well within the upper-limit that the theoretical model could reach. It is also important to note that the RGB-bump is not the only stage for inhabitation of Li-rich giants, many Li-rich giants have been reported in various stages by previous work, including the core He-burning phase, which is very close to the RGB-bump region on the H-R diagram. Although it is not preferred by our data, if our star occupies this stage, a new scenario

will be in urgent need for interpreting such high Li abundance.

References

- [1] Brown, J. A., Sneden, C., Lambert, D. L., Dutchover, E., Jr. A search for lithium-rich giant stars. *Astrophys. J. (Suppl.)* **71**, 293-322 (1989).
- [2] Iben, I., Jr. Stellar evolution. VI. Evolution from the main sequence to the red-giant branch for stars of mass $1 M_{\odot}$, $1.25 M_{\odot}$, and $1.5 M_{\odot}$. *Astrophys. J.* **147**, 624 (1967).
- [3] Cyburt, R. H., Fields, B. D., Olive, K. A., Yeh, T.-H. Big bang nucleosynthesis: Present status. *Rev. Mod. Phys.* **88**, 015004 (2016).
- [4] Spite, M., & Spite, F. Lithium abundance at the formation of the Galaxy. *Nature* **297**, 483-485 (1982).
- [5] Tajitsu, A., Sadakane, K., Naito, H., Arai, A., Aoki, W. Explosive lithium production in the classical nova V339 Del (Nova Delphini 2013). *Nature* **518**, 381-384 (2015).
- [6] Sackmann, I.-J., & Boothroyd, A. I. Creation of ^7Li and Destruction of ^3He , ^9Be , ^{10}B , and ^{11}B in low-mass red giants, due to deep circulation. *Astrophys. J.* **510**, 217-231 (1999).
- [7] Denissenkov, P. A., & Herwig, F. Enhanced extra mixing in low-mass red giants: Lithium production and thermal stability. *Astrophys. J.* **612**, 1081-1091 (2004).
- [8] Charbonnel, C., & Lagarde, N. Thermohaline instability and rotation-induced mixing. I. Low- and intermediate-mass solar metallicity stars up to the end of the AGB. *Astron. Astrophys.* **522**, A10 (2010).
- [9] Wallerstein, G., & Sneden, C. A K giant with an unusually high abundance of lithium - HD 112127. *Astrophys. J.* **255**, 577-584 (1982).
- [10] Monaco, L. *et al.* Lithium-rich giants in the Galactic thick disk. *Astron. and Astrophys.* **529**, A90 (2011).
- [11] Kirby, E. N., Fu, X., Guhathakurta, P., Deng, L. Discovery of super-Li-rich red giants in dwarf spheroidal galaxies. *Astrophys. J.* **752**, L16 (2012).
- [12] Martell, S. L., & Shetrone, M. D. Lithium-rich field giants in the Sloan Digital Sky Survey. *Mon. Not. R. Astron. Soc.* **430**, 611-620 (2013).
- [13] Adamów, M., Niedzielski, A., Villaver, E., Wolszczan, A., Nowak, G. The Penn State - Toruń Centre for Astronomy Planet Search stars. II. Lithium abundance analysis of the red giant clump sample. *Astron. Astrophys.* **569**, A55 (2014).
- [14] Casey, A. R. *et al.* The Gaia-ESO Survey: revisiting the Li-rich giant problem. *Mon. Not. R. Astron. Soc.* **461**, 3336-3352 (2016).
- [15] Balachandran, S. C., Fekel, F. C., Henry, G. W., Uitenbroek, H. Two K giants with supermetallic lithium abundances: HDE 233517 and HD 9746. *Astrophys. J.* **542**, 978-988 (2000).
- [16] Reddy, B. E., & Lambert, D. L. Three Li-rich K giants: IRAS 12327-6523, 13539-4153, and 17596-3952. *Astron. J.* **129**, 2831-2835 (2005).
- [17] Kumar, Y. B., Reddy, B. E., Lambert, D. L. Origin of lithium enrichment in K giants. *Astrophys. J.* **730**, L12 (2011).
- [18] de La Reza, R., & da Silva, L. Lithium abundances in strong lithium K giant stars: LTE and non-LTE analyses. *Astrophys. J.* **439**, 917-927 (1995).
- [19] Kumar, Y. B., & Reddy, B. E. HD 77361: A new case of super Li-rich K giant with anomalous low $^{12}\text{C}/^{13}\text{C}$ ratio. *Astrophys. J.* **703**, L46-L50 (2009).
- [20] Ruchti, G. R., *et al.* Metal-poor lithium-rich giants in the Radial Velocity Experiment Survey. *Astrophys. J.* **743**, 107 (2011).
- [21] Carlberg, J. K. *et al.* The puzzling Li-rich red giant associated with NGC 6819. *Astrophys. J.* **802**, 7 (2015).
- [22] Lind, K., Asplund, M., Barklem, P. S. Departures from LTE for neutral Li in late-type stars. *Astron. Astrophys.* **503**, 541-544 (2009).
- [23] Aguilera-Gómez, C., Chanamé, J., Pinsonneault, M. H., Carlberg, J. K. On Lithium-rich red giants: Engulfment on the giant branch of Trumpler 20. *Astrophys. J.* **833**, L24 (2016).
- [24] Kirby, E. N., *et al.* Lithium-rich giants in globular clusters. *Astrophys. J.* **819**, 135 (2016).
- [25] Silva Aguirre, V., *et al.* Old puzzle, new insights: a lithium-rich giant quietly burning helium in its core. *Astrophys. J.* **784**, L16 (2014).
- [26] Gaia Collaboration *et al.* Gaia data release 1. Summary of the astrometric, photometric, and survey properties. *Astron. Astrophys.* **595**, A2 (2016).
- [27] Alexander, J. B. A possible source of lithium in the atmospheres of some red giants. *The Observatory* **87**, 238-240 (1967).
- [28] Cameron, A. G. W., & Fowler, W. A. Lithium and the s-process in red-giant stars. *Astrophys. J.* **164**, 111 (1971).
- [29] Cyburt, R. H. *et al.* The JINA REACLIB Database: Its recent updates and impact on Type-I X-ray Bursts. *Astrophys. J. (Suppl.)* **189**, 240-252 (2010).
- [30] Busso, M., Wasserburg, G. J., Nollett, K. M., Calandra, A. Can extra mixing in RGB and AGB stars be attributed to magnetic mechanisms? *Astrophys. J.* **671**, 802-810 (2007).

Acknowledgements This research was supported by National Key Basic Research Program of China 2014CB845700, the National key Research and Development Project of China 2016YFA0400502, and the National Natural Science Foundation of China under grant Nos. 11390371, 11603037, 11473033, 11490560, 11505117, 11573032, 11605097. Guoshoujing Telescope (LAMOST) is a National Major Scientific Project built by the Chinese Academy of Sciences. Funding for the project has been provided by the National Development and Reform Commission. LAMOST is operated and managed by the National Astronomical Observatories, Chinese Academy of Sciences. This work is supported by the Astronomical Big Data Joint Research Center, co-founded by the National Astronomical Observatories, Chinese Academy of Sciences and the Alibaba Cloud. This research uses data obtained through the Telescope Access Program (TAP). The authors acknowledge Dr. James Wicker for proof-reading the manuscript. We acknowledge the use of *Gaia* and WISE data, and of VizieR catalogue access tool.

Author contributions H.-L.Y., J.-R.S. and G.Z. proposed and designed this study. H.-L.Y. and J.-R.S. led the data analysis with the contributions from Y.-T.Z., Q.G., J.-B.Z., and Z.-M.Z.. Y.-S.C., E.-T.L., S.Z., Z.-H.L., B.G., and W.-P.L. performed the nuclear calculations. S.-L.B. and Y.-Q.W. calculated the evolutionary models and tracks. H.-N.L. carried out the observation. All the authors discussed the results and contributed to the writing of the manuscript.

Author Information Reprints and permissions information is available at www.nature.com/reprints. The authors declare no competing financial interests. Readers are welcome to comment on the online version of the paper. The data that support the plots within this paper and other findings of this study are available from the corresponding author upon reasonable request. Correspondence and requests for materials should be addressed to J.-R.Shi (sjr@nao.cas.cn) or G. Zhao (gzhao@nao.cas.cn).

Methods

Data Reduction. We followed the standard procedure for data reduction with an Interactive Data Language (IDL) package, which was originally designed for the FOCES spectrograph^[31]. The instrumental response and background scatter light were considered during the reduction, and cosmic rays and bad pixels were removed carefully. The resulting spectrum has a signal-to-noise ratio of ~ 160 at 6707.8 Å.

Deriving the Stellar Parameters. We first combined three iron (Fe) line lists^[32, 33, 34] and calibrated 213 lines out of 257 with the solar spectrum^[35]. Then we eliminated those seriously blended or poorly recognized lines seen from the spectrum of TYC 429-2097-1, as well as the lines that are too strong (> 120 mÅ) or too weak (< 20 mÅ). Finally, 57 Fe I and 12 Fe II lines are used as the parameter indicators. The effective temperature (T_{eff}) is derived from the excitation equilibrium of Fe I lines with excitation energy (E_{exc}) greater than 2.0 eV^[36]. The surface gravity ($\log g$) is approached by equalizing the two sets of Fe abundances obtained from Fe I and Fe II lines, respectively. Statistically, the Fe abundance derived from each individual Fe I line and the equivalent width (EW) from the same Fe I line will be mutually independent if the micro-turbulence velocity (ξ_t) is correctly set. Using this trick, we can obtain ξ_t , and then the metallicity ([Fe/H]) can be settled simultaneously if all the mentioned constraints are achieved. All the Fe abundances are derived from NLTE analysis with the MARCS atmospheric models^[37] since it has been suggested that Fe I lines suffer a non-negligible NLTE effect^[33]. The procedure of this approach is much more like an iteration. We started with the results from LAMOST pipeline as the initial input, and then by calculating MARCS models and adjusting the stellar parameters step by step, we finally end up with a self-consistent solution. Supplementary Figure 3 shows the derived Fe abundances from individual lines as functions of their EWs (upper panel) and E_{exc} (lower panel). Based on the experience of our previous work using the similar spectroscopic method, the errors for T_{eff} , $\log g$, [Fe/H] and ξ_t are estimated to be ± 80 K, ± 0.10 dex, ± 0.06 dex and ± 0.10 km s⁻¹, respectively.

Determination of the Elemental Abundances. For all the species discussed in this paper, we use the spectrum synthesis method to derive their abundances. The theoretical profiles of the corresponding lines are calculated based on the MARCS model^[37]. An interactive IDL code Spectrum Investigation Utility (SIU) was applied to calculate the synthetic line profiles. The coupled radiative transfer and statistical equilibrium equations for the NLTE calculation were solved following the efficient method with a revised DETAIL program based on the accelerated lambda iteration, we refer readers to Mashonkina *et al.* (2011) for a more detailed description of this method^[33]. The resulting departure files are transferred into SIU for NLTE line synthesis. The solar iron abundance of $\log \epsilon_{\text{Fe}} = 7.5$ was assumed in our work.

In the abundance analysis of Li, the resonance line at 6707.8 Å, the subordinate line at 6103.6 Å and the line at 8126.3 Å^[38] were used to derive the Li abundance. Although the line at 8126.3 Å is blended with two telluric lines, it shows similar result to those derived from the resonance and subordinate lines. The final Li abundance is determined by averaging the results from these three lines. It is noted by many previous studies that the NLTE corrections are important for strong lines. In general, the NLTE correction for Li is not large for the ‘Li-normal’ stars, however it will significantly increase for Li-rich objects,

especially for the strong resonance line at 6707.8 Å. In the very extreme cases (such as ours), the local thermodynamic equilibrium (LTE) theoretical profile of 6707.8 Å could be saturated at the core. Therefore, the NLTE effects were taken into consideration in our abundance analysis for Li. For the NLTE analysis, we applied the same atomic model and line data as those presented in Shi *et al.* 2007^[39]. The carbon abundances were derived from the C I line at 5086 Å, and the C₂ line at 5135 Å^[40]. The nitrogen lines were either blended or too weak in our spectrum, so we turned to the CN band near 8003.5 Å to estimate the N abundance by fixing C to the value we just derived. Then the carbon isotopic ratio was determined by adjusting the contributions from ¹²C and ¹³C until we get the best fit to the CN band observed profile. The determination of α -abundance (Mg, Si, and Ca) with NLTE analysis was based on a series of previous work^[41, 42, 43]. The final α -abundance was obtained by averaging the abundances obtained from those elements. We also derived abundances of several other elements, and they can be found in Supplementary Table 1.

The error of the Li abundance was estimated by changing the stellar parameters (namely T_{eff} , $\log g$, and [Fe/H]) within their error ranges and calculating the corresponding variations on the abundance. The result of this test is presented in Supplementary Table 2. It is clear that the Li abundance is more sensitive to the variation of T_{eff} than that of $\log g$ or [Fe/H]. A change of 80 K on T_{eff} will result in a variation of ~ 0.09 dex for the Li abundance. Thus, we adopted the variation caused by the error of the effective temperature as the uncertainty for each Li I line, which is ± 0.09 , ± 0.09 , and ± 0.08 for the lines of 6707.8 Å, 6103.6 Å, and 8126.3 Å respectively. The error of the final Li abundance is obtained by calculating the standard deviation of abundances derived from the three lines. For the other elements, if more than three lines are used for the abundance determination, we calculate their standard deviation and compare it to the error caused by the uncertainties of the stellar parameters, and the larger one was adopted as the final error. A few of species such as ¹²C/¹³C ratio were not suitable for the above analysis, we estimated their errors by giving the upper- and lower- limit of the best-fit to the profile.

Maximum Likelihood Method and Evolutionary Stage. The likelihood function is expressed following Basu *et al.*^[44], which is defined as:

$$L = L_{P_{\text{obs}1}} L_{P_{\text{obs}2}} L_{P_{\text{obs}3}} \cdots, \quad (1)$$

where P_{obs} is the observed parameter (e.g., T_{eff}) and

$$L_{P_{\text{obs}}} = \frac{1}{\sqrt{2\pi}\sigma_{P_{\text{obs}}}} \exp\left(-\frac{(P_{\text{obs}} - P_{\text{model}})^2}{2\sigma_{P_{\text{obs}}}^2}\right). \quad (2)$$

The normalized probability of each model p_i is expressed as

$$p_i = \frac{L_i}{\sum_{i=1}^{N_m} L_i}, \quad (3)$$

where L_i is the likelihood function of the i th model and N_m is the total amount of the models. The probability is integrated from the boundary constrained by 3σ error range of the observed parameters. Thus, the maximum value of the integrated probability is 0.5, and the best-fitted parameters are obtained from this probability^[45].

The grid of evolutionary models for calculating the likelihood are generated from MESA^[46] code. The grid covers a wide-range of mass from 0.6–3.0 M_{\odot} with a 0.02 M_{\odot} interval on mass and a 0.005 interval on metallicity (Z). The evolution tracks are constructed from the pre-main sequence to the asymptotic giant

branch (AGB) phase. For generating the grid, the initial parameter setup was mostly as same as described in Paxton *et al.* 2011^[46] except for the solar chemical abundance $(Z/X)_\odot$. We adopted $(Z/X)_\odot = 0.0229$ ^[47] because calibrated solar model with this mixture fits the internal structures from helioseismic inversion^[48] slightly better than the others^[49]. The MESA ρ - T tables are based on an updated version of Rogers & Nayfonov tables^[50]. Ferguson *et al.*^[51] extended the opacity for the solar composition to the low-temperature case in 2015, and we adopted their results in our computation. The stellar metallicity was transferred into ‘metal’ abundance Z_{init} , from where the hydrogen and helium abundances (X_{init} and Y_{init}) were calculated.

To obtain the luminosity and $\log g_{\text{Gaia}}$ from the parallax, we first calculated the bolometric magnitude for the absolute V magnitude by $M_{\text{bol}} = V_{\text{mag}} + BC + 5 \log \pi - A_V$ (in this equation, π is used in the unit of arcsec), where the bolometric correction BC was computed following Alonso *et al.*^[52] and A_V was estimated by the Galactic extinction map presented by Schlafly & Finkbeiner at 2011^[53] (all values that were need for the calculation were presented in Supplementary Table). We calculated the luminosity using the relation of $M_{\text{bol}} - M_{\text{bol}\odot} = -2.5 \log(\frac{L_{\text{Gaia}}}{L_\odot})$. Finally, the $\log g_{\text{Gaia}}$ was determined following the fundamental relation $\log g = \log g_\odot + \log(\frac{M}{M_\odot}) + 4 \log(\frac{T_{\text{eff}}}{T_{\text{eff}\odot}}) + 0.4(M_{\text{bol}} - M_{\text{bol}\odot})$, where $\log g_\odot = 4.44$, $M = 1.36 M_\odot$, $T_{\text{eff}\odot} = 5777 \text{ K}$, and $M_{\text{bol}\odot} = 4.74 \text{ mag}$. The errors were given via the uncertainty transfer formula assuming that the errors were contributed by the uncertainty of the Gaia parallax.

Parametric Calculation of Internal Li-enriching. During the RGB stage of a low-mass star, we introduced the ‘extra-mixing’ or the ‘circulation process’ after the H-burning shell has erased the chemical discontinuity left behind by FDU, signatred by the bump of the luminosity function in RGB. We followed the parameterization of Nollett *et al.*^[54] to perform the parametric calculations using \dot{M} , T_p , f_d and f_u as free parameters.

The basic assumptions are described as follows. The EM is a process of meridional circulation in the radiative zone of low-mass red giant stars, the path of mass flow looks like a ‘conveyor belt’. A parcel of material with the initial abundance composition $Y_i^E(0)$ at the base of the convective envelope circulates downward through the radiative zone structure and finally returns to the envelope with newly processed abundance composition Y_i^P . The velocity of the sampled material can be expressed as $dr/dt = \dot{M}/f4\pi r^2\rho$, where f is equal to f_d (or f_u) for the downward (or upward) circulation, and the density ρ is a function of radius r , governed by the stellar structure. The stellar structure, \dot{M} and Δ specify as functions of time, the conditions of temperature T and density ρ where the material pass through.

The computing code integrates the network of reactions of the hydrogen burning chain by following the circulation trajectory. The nuclear reaction rates adopted are from NACRE^[55] except for two rates, the updated rate of ${}^7\text{Be}(p, \gamma){}^8\text{B}$ is from Du *et al.* 2015^[56] and the rate of ${}^7\text{Be}(e, \nu){}^7\text{Li}$ from the JINA database. The convective overturn-time of the envelope is set to $\sim 1 \text{ yr}$, which is a good approximation in the sense that the mixing between the processed material and the convective envelope is instantaneous. The abundance of the i -th nucleus changes in the envelope during the transport is due to the nucleosynthesis and the material replacement, and this corresponds to integrating $\dot{Y}_i^E = (\dot{M}/M_E)(Y_i^P - Y_i^E(0))$ ^[54], where M_E is the mass of convective envelope. In order to obtain the RGB stellar structure, including in particular the initial abundance composition

in the envelope and the distributions of temperature and density in the radiative zone, we calculated the stellar evolution model for $M = 1.36 M_\odot$ by the MESA code. The initial abundance of ${}^7\text{Li}$ in the sample material at the base of the envelope is $\sim 1.024 \times 10^{-11}$ ($A(\text{Li})=1.86$) obtained from the present stellar evolutionary model calculation, and the ${}^7\text{Li}$ abundance may increase to a level of $A(\text{Li})$ exceeding 4 in the processed material when the mass circulation finishes.

During the downward mass circulation, the abundance of ${}^7\text{Be}$ increases quickly because the construction reaction ${}^3\text{He}({}^4\text{He}, \gamma){}^7\text{Be}$ wins against the destruction reaction ${}^7\text{Be}(p, \gamma){}^8\text{B}$, and the maximum yield of ${}^7\text{Be}$ is around the turning point of the mass circulation, where the temperature reaches the highest value T_p . In contrast, the production change of ${}^7\text{Li}$ behaves rather dramatically during the downward mass circulation due to the complex competition between the production reaction ${}^7\text{Be}(e^-, \nu){}^7\text{Li}$ and the destruction reactions ${}^7\text{Li}(p, \gamma){}^8\text{Be}$ and ${}^7\text{Li}(p, \alpha){}^4\text{He}$. The abundance of ${}^7\text{Li}$ drops suddenly at about 200 yrs of the processing time as the rates of destruction reactions increase quickly with increasing temperature, and the ${}^7\text{Li}$ abundance keeps very low during the downward mass circulation although it increases slightly after about 230 yrs due to the decay of fast growing abundant ${}^7\text{Be}$. In contrast, the abundance of ${}^7\text{Li}$ increases sharply during the upward mass circulation due to the fast decreasing of the destruction reaction rates of ${}^7\text{Li}$ as the temperature decreases quickly. The processed abundance Y_{Li}^P finally reaches a super-high-level of $A(\text{Li})=4.506$. The abundance of ${}^7\text{Li}$ in the envelope contains the contributions of the mass circulation and mass replacement processes, and the total processing time can be estimated as M_E/\dot{M} , which is about $2.1 \times 10^4 \text{ yrs}$ by using the average value of the envelope mass for this RGB star.

The Projected Rotational Velocity. Following the assumption of Bruntt *et al.*^[57], the external broadening of the line profile was assumed to be contributed from the stellar rotation, instrumental broadening, and macro-turbulence. The projected rotational velocity ($v \sin i$) was derived by using five isolated iron lines at 6151 Å, 6229 Å, 6380 Å, 6703 Å, and 6810 Å. The instrumental broadening was calculated from fitting the emission lines of the arc lamp with a Gaussian profile. The macro-turbulence velocity was estimated using the relation of Hekker *et al.*^[58], which is a function of T_{eff} and $\log g$. Then we calculated a set of the theoretical spectra broadened with different rotational velocities, and $v \sin i$ was determined by finding the best-fit to the observed iron line profiles.

References

- [31] Pfeiffer, M. J., Frank, C., Baumüller, D., Fuhrmann, K., Gehren, T. FOCES - a fibre optics Cassegrain Echelle spectrograph. *Astron. Astrophys. Suppl.* **130**, 381-393 (1998).
- [32] Takeda, Y., Sato, B., Kambe, E., Sadakane, K., Ohkubo, M. Spectroscopic determination of stellar atmospheric parameters: Application to mid-F through early-K dwarfs and Ssubgiants. *Publ. Astron. Soc. Jpn.* **54**, 1041-1056 (2002).
- [33] Mashonkina, L., Gehren, T., Shi, J.-R., Korn, A. J., Grupp, F. A non-LTE study of neutral and singly-ionized iron line spectra in 1D models of the Sun and selected late-type stars. *Astron. Astrophys.* **528**, A87 (2011).
- [34] Carlberg, J. K., Cunha, K., Smith, V. V., Majewski, S. R. Observable signatures of planet accretion in red giant stars. I. rapid rotation and light element replenishment. *Astrophys. J.* **757**, 109 (2012).

- [35] Kurucz, R. L., Furenlid, I., Brault, J., Testerman, L. Solar flux atlas from 296 to 1300 nm. *National Solar Observatory Atlas*, 25–33, *Sunspot, New Mexico: National Solar Observatory* (1984).
- [36] Sitnova, T. *et al.* Systematic non-LTE study of the $-2.6 < [\text{Fe}/\text{H}] < 0.2$ F and G dwarfs in the solar neighborhood. I. stellar atmosphere parameters. *Astrophys. J.* **808**, 148 (2015).
- [37] Gustafsson, B. *et al.* A grid of MARCS model atmospheres for late-type stars. I. Methods and general properties. *Astron. Astrophys.* **486**, 951-970 (2008).
- [38] Adamów, M. *et al.* Tracking advanced planetary systems (TAPAS) with HARPS-N II. super Li-rich giant HD 107028. *Astron. Astrophys.* **581**, A94 (2015).
- [39] Shi, J. R., Gehren, T., Zhang, H. W., Zeng, J. L., Zhao, G. Lithium abundances in metal-poor stars. *Astron. Astrophys.* **465**, 587-591 (2007).
- [40] Alexeeva, S. A., & Mashonkina, L. I. Carbon abundances of reference late-type stars from 1D analysis of atomic C I and molecular CH lines. *Mon. Not. R. Astron. Soc.* **453**, 1619-1631 (2015).
- [41] Mashonkina, L. Astrophysical tests of atomic data important for the stellar Mg abundance determinations. *Astron. Astrophys.* **550**, A28 (2013).
- [42] Zhang, J., Shi, J., Pan, K., Allende Prieto, C., Liu, C. NLTE analysis of high-resolution H-band spectra. I. neutral silicon. *Astrophys. J.* **833**, 137 (2016).
- [43] Mashonkina, L., Korn, A. J., Przybilla, N. A non-LTE study of neutral and singly-ionized calcium in late-type stars. *Astron. Astrophys.* **461**, 261-275 (2007).
- [44] Basu, S., Chaplin, W. J., Elsworth, Y. Determination of stellar radii from asteroseismic data. *Astrophys. J.* **710**, 1596-1609 (2010).
- [45] Wu, Y.-Q. *et al.* Stellar parameters of main sequence turn-off star candidates observed with LAMOST and Kepler. *Res. Astron. Astrophys.* **17**, 5 (2017).
- [46] Paxton, B. *et al.* Modules for experiments in stellar astrophysics (MESA). *Astrophys. J. Suppl.* **192**, 3 (2011).
- [47] Grevesse, N., & Sauval, A. J. Standard solar composition. *Space Sci. Rev.* **85**, 161-174 (1998).
- [48] Bi, S. L., Li, T. D., Li, L. H., Yang, W. M. Solar models with revised abundance. *Astrophys. J.* **731**, L42 (2011).
- [49] Asplund, M., Grevesse, N., Sauval, A. J., Scott, P. The chemical composition of the Sun. *Annu. Rev. Astron. Astrophys.* **47**, 481-522 (2009).
- [50] Rogers, F. J., & Nayfonov, A. Updated and expanded OPAL equation-of-state tables: Implications for helioseismology. *Astrophys. J.* **576**, 1064-1074 (2002).
- [51] Ferguson, J. W. *et al.* Low-temperature opacities. *Astrophys. J.* **623**, 585-596 (2005).
- [52] Alonso, A., Arribas, S., Martínez-Roger, C. The effective temperature scale of giant stars (F0-K5). II. empirical calibration of T_{eff} versus colours and $[\text{Fe}/\text{H}]$. *Astron. Astrophys. Suppl.* **140**, 261-277 (1999).
- [53] Schlafly, E. F., & Finkbeiner, D. P. Measuring reddening with Sloan Digital Sky Survey stellar spectra and recalibrating SFD. *Astrophys. J.* **737**, 103 (2011).
- [54] Nollert, K. M., Busso, M., Wasserburg, G. J. Cool bottom processes on the thermally pulsing asymptotic giant branch and the isotopic composition of circumstellar dust grains. *Astrophys. J.* **582**, 1036-1058 (2003).
- [55] Angulo, C. *et al.* A compilation of charged-particle induced thermonuclear reaction rates. *Nucl. Phys. A* **656**, 3-183 (1999).
- [56] Du, X. *et al.* Determination of astrophysical ${}^7\text{Be}(p,\gamma){}^8\text{B}$ reaction rates from the ${}^7\text{Li}(d,p){}^8\text{Li}$ reaction. *Sci. China-Phys. Mech. Astron.*, **58**, 062001 (2015).
- [57] Bruntt, H. *et al.* Accurate fundamental parameters for 23 bright solar-type stars. *Mon. Not. R. Astron. Soc.*, **405**, 1907 (2015).
- [58] Hekker, S., Meléndez, J. Precise radial velocities of giant stars. III. Spectroscopic stellar parameters. *Astron. Astrophys.*, **475**, 1003 (2007).

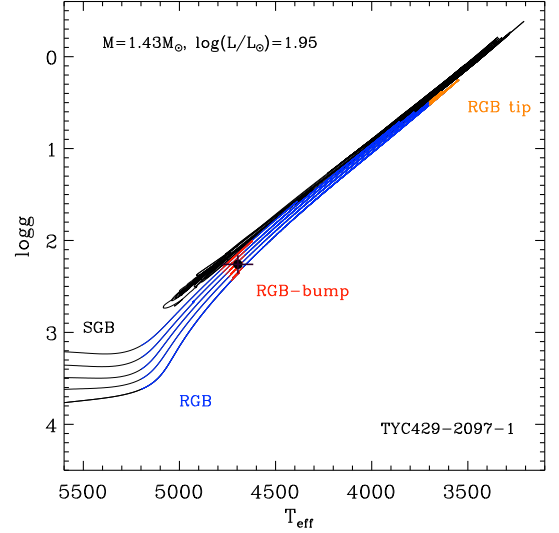
Supplementary Information

Supplementary Table 1. Other information of TYC 429-2097-1

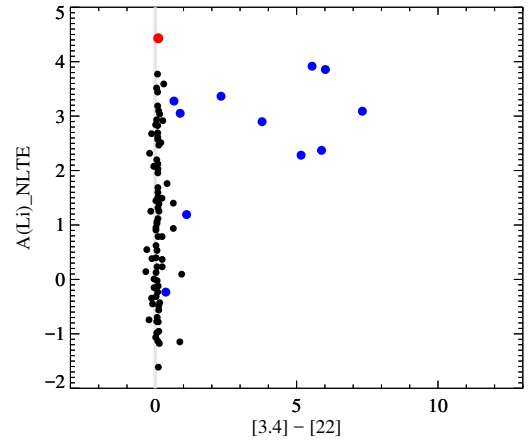
Property		Value
Position (J2000)	R.A.	17 : 53 : 46.07
	DEC.	06 : 42 : 41.20
	l	32.4111
	b	15.8647
V_{mag}	(mag)	11.27 (UCAC4)
Gaia parallax π	(milli-arcsec)	0.73 ± 0.24
A_V	(mag)	0.47
BC	(mag)	-0.385
M_{bol}	(mag)	-0.27
$[C/Fe]$		-0.02 ± 0.10
$[N/Fe]$		0.45 ± 0.10
$[Mg/Fe]$		0.23 ± 0.05
$[Si/Fe]$		0.19 ± 0.01
$[Ca/Fe]$		0.16 ± 0.06

Supplementary Table 2. The variation of Li abundance caused by the uncertainties of stellar parameters

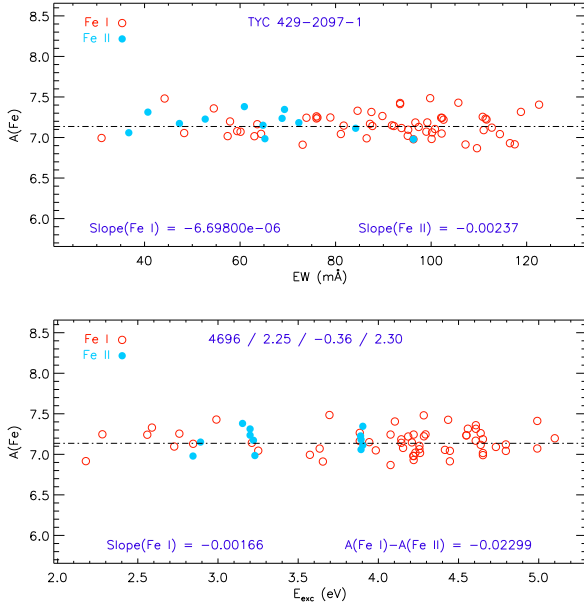
Wavelength	ΔT_{eff}	$\Delta \log g$	$\Delta [Fe/H]$
	80 K	0.10 dex	0.06 dex
6103.6 Å	0.09	0.02	0.07
6707.8 Å	0.09	0.03	0.06
8126.3 Å	0.08	0.01	0.07



Supplementary Figure 1. The corresponding evolutionary tracks computed from the MESA code for TYC 429-2097-1. The mass range of the tracks is from $1.0 M_{\odot}$ (bottom) to $1.8 M_{\odot}$ (top), with an interval of $0.2 M_{\odot}$. The evolutionary stages for each track are indicated with different colors, namely: ‘black’ – SGB, ‘dark blue’ – RGB, ‘red’ – RGB-bump and ‘orange’ – RGB tip. The position of TYC 429-2097-1 is indicated with a black dot. The error bars indicate the uncertainties in T_{eff} and $\log g$, which are adopted to be ± 80 K and 0.10 dex from our stellar parameters determination method.



Supplementary Figure 2. The IR-excess diagram for TYC 429-2097-1. TYC 429-2097-1 is indicated with a red dot, while the other stars are from Rebull et al. 2015. The horizontal line at $A(Li) = 1.5$ shows the adopted division between Li-rich and normal stars, and the vertical line at $[3.4] - [22] = 0$ indicates the photospheric locus. The blue dots denote the objects with strong IR-excess, while the black dots represent the stars with no significant IR-excess.



Supplementary Figure 3. The determination of the stellar parameters. The figure shows the absolute NLTE abundance from lines of Fe I (red open circle) and Fe II (blue dots) in TYC 429-2097-1 as functions of their EWs (top panel) and E_{exc} (bottom panel). The slopes are indicated in the corresponding panel. The mean $A(\text{Fe})$ averaged from Fe I and Fe II lines is shown with a dash-dotted line in both panels. The final stellar parameters are denoted in the sequence of T_{eff} (K), $\log g$, $[\text{Fe}/\text{H}]$, and ξ_t (km s^{-1}) in the bottom panel.